Supporting Information for

"Policy-relevant assessment of urban CO_2 emissions"

Thomas Lauvaux[1,2], Kevin R. Gurney[3], Natasha L. Miles[2], Kenneth J. Davis[2], Scott J. Richardson[2], Aijun Deng[4], Brian J. Nathan[5], Tomohiro Oda[6,7], Jonathan A. Wang[8], Lucy Hutyra[9], and Jocelyn Turnbull[10,11]

[1] Laboratoire des Sciences du Climat et de l'Environnement, CEA, CNRS, UVSQ/IPSL, Université Paris-Saclay, Orme des Merisiers, 91191 Gif-sur-Yvette cedex, France

[2] Department of Meteorology and Atmospheric Science, The Pennsylvania State University, University Park, PA 16802, USA

[3] School of Informatics, Computing, and Cyber Systems, Northern Arizona University, Flagstaff, AZ, USA

[4] Utopus Insights, Valhalla, NY, USA

[5] Aix-Marseille Université, OSU Pytheas, Institut Méditerranéen de Biodiversité et d'Ecologie Marine et Continentale, Campus Aix Technopôle de l'environnement Arbois Méditerranée, Aix-en-Provence, France

[6] Global Modeling and Assimilation Office, NASA Goddard Space Flight Center, Greenbelt, MD,USA

[7] Goddard Earth Sciences Technology and Research, Universities Space Research Association,Columbia, MD, USA

[8] University of California, Irvine, CA, USA

[9] Boston University, Boston, MA, USA

[10] Rafter Radiocarbon Laboratory, GNS Science, Lower Hutt, New Zealand

[11] CIRES, University of Colorado at Boulder, CO.

Corresponding author: Thomas Lauvaux
Email: thomas.lauvaux@lsce.ipsl.fr

This PDF file includes:

Supplementary text S1 to S11
Figures S1 to S9
SI References

Text S1. Atmospheric modeling system with data assimilation.
Text S2. Adjoint modeling with backward trajectories.

Text S1. Atmospheric modeling system with data assimilation. The atmospheric dynamics was simulated using the Weather Research and Forecasting model (WRF; **1**) assimilating meteorological observations continuously using the Four Dimensional Data Assimilation system (FDDA) originally developed for MM5 (**2**) and later implemented into WRF (**3**). The WRF configuration for the model physics used here was based on previous numerical modeling studies (**4**) using (1) the single-moment three-class simple ice scheme for microphysical processes, (2) the Kain-Fritsch scheme for cumulus parameterization on the 9 km grid, (3) the Rapid Radiative Transfer Model for longwave atmospheric radiation and the Dudhia scheme for shortwave atmospheric radiation, (4) the turbulent kinetic energy (TKE)-predicting Mellor-Yamada-Nakanishi-Niino (MYNN) Level 2.5 turbulent closure scheme for the turbulence parameterization in the planetary boundary layer (PBL), and (5) the five-layer thermal diffusion scheme for representation of the interaction between the land surface and the atmospheric surface layer. Assimilation of the wind field is applied through all model layers, but nudging of the mass fields (temperature and moisture) is only allowed above the model-simulated PBL so that the PBL structure produced by the model is dominated by the model physics. Similar to the configuration described in a previous study (**5**), World Meteorological Organization (WMO) observations were assimilated into the WRF-FDDA system to produce a dynamic analysis, blending the model simulations and the observations to produce the most accurate meteorological conditions possible to simulate the atmospheric CO2 concentrations in space and time throughout the Indianapolis region. The WRF model grid configuration used for this demonstration is comprised of three grids: 9 km, 3 km, and 1 km (cf. Figure 1 for the 3 km and 1 km grids), all of which are co-centered over Indianapolis, Indiana. The 9 km grid, with a mesh of 100 × 100 grid points, contains the eastern part of the U.S. Midwest. The 3 km grid, with a mesh of 99 × 99 grid points, contains the southern part of the state of Indiana. The 1 km grid, with a mesh of 87 × 87, covers the metropolitan area of Indianapolis and the eight counties surrounding Marion county. Fifty-nine vertical terrain-following layers are used, with the center point of the lowest model layer located ~6 m above ground level (AGL). The thickness of the layers increases gradually with height, with 25 layers below 850 hPa (~1550 m AGL). Model performances have been extensively studied (**3**) including surface wind conditions and vertical mixing heights.

Text S2. Adjoint modeling with backward trajectories. The Lagrangian Particle Dispersion Model (LPDM; **6**) is used as the adjoint model of the WRF-FDDA modeling system. The coupling between WRF-FDDA and LPDM has been described in previous work (**5**) with the same configuration used in this study. Particles are released from the receptors in a backward in time mode with the wind fields and the turbulence generated by the Eulerian model WRF-FDDA. In a backward in time mode, particles are released from the measurement locations and travel to the surface and the boundaries. Every 20 s, 35 particles are released at the position of the towers, which corresponds to 6,300 particles per hour per measurement site (or receptor). The dynamical fields in LPDM are forced by mean horizontal winds (u, v, w), potential temperature and turbulent kinetic energy (TKE) from WRF-FDDA. Particle locations and times are gridded to generate 1-km tower footprints, the linear solution of the relationship between concentration measurements and surface fluxes. The formalism for inferring source-receptor relationships from particle distributions is described in previous studies (**7**). For an assessment of the adjoint system, the LPDM model performances have been recently evaluated and compared to other back-trajectory Lagrangian models over the Barnett shale using methane (CH_4) mixing ratios collected during ten aircraft flights (**8**). Daily CH_4 emissions computed with aircraft footprints from WRF-FDDA coupled to LPDM was the closest to the high-resolution CH4 emissions inventory over the Barnett shale among eight modeling systems, with a day-to-day standard deviation of 0.32 (WRF-LPDM) and a mean emission estimate agreeing within 25% of the inventory.

Text S3. Building-level sectoral fossil fuel CO_2 gridded emissions: Hestia. The Hestia CO_2 emission product (**9**) was coupled to the LPDM footprints to simulate the CO_2 atmospheric mixing ratios over and around Indianapolis. The Hestia product combines observations and modeling to produce CO_2 emissions from the combustion of fossil fuels. A wide range of data sources are used to quantify emissions at the scale of individual buildings and road segments, including local traffic monitoring, property tax assessor data, power plant emissions monitoring, and air quality pollution reporting. The data product includes some spatial and temporal proxies to attain hourly emissions at fine spatial scales for Marion County and the eight counties that surround Marion County. The space and time patterns are generated for the year 2011. Emissions for 2012 to 2015 reflect the application of scale factors derived from the Department of Energy (DOE) Energy Information Administration (EIA) fuel statistics specific to sector and fuel type. Hence, the magnitude of emissions change over the time period but the sub-county spatial structure remains fixed. Furthermore, the submonthly time structure in all sectors other than power production are represented by fixed time cycles derived from multiple years of monitoring data. For example, the onroad CO_2 emissions reflect a spatially explicit use of a mean weekly cycle (7 day cycle within a given month) and mean diurnal cycle (24 h cycle within a given week). The emissions available for each of the eight economic sectors were aggregated from the initial building-level product down to the 1-km resolution footprint grid, covering Marion County and the eight surrounding counties. Figure S1 shows the CO_2 emissions in ktC km^{-2}

Text S4. Disaggregated national CO_2 Emissions: ODIAC. The Open-Source Data Inventory for Anthropogenic CO_2 (ODIAC) emission data (**10**) was used in this study as an alternative prior for the optimization system. ODIAC was originally designed to provide spatially-explicit emissions of CO_2 anywhere over the globe for global- and regional-scale applications. Urban applications, beyond the initial scope of ODIAC, are used to evaluate the importance of the spatial resolution of the prior emissions at fine scales. Currently, nightlight satellite data used as a proxy to distribute national emissions can describe urban emissions at a resolution of about 3 km. The version of the ODIAC emission data used in this study is based on emission estimates updated using the Carbon Dioxide Information Analysis Center (CDIAC) global and national fossil fuel emission estimates (http://cdiac.ornl.gov/trends/emis/meth_reg.html; last access 27 March 2015) and annual BP statistical review of world energy (http://www.bp.com/en/global/corporate/about-bp/energy-economics/statistical-review-of-world-energy/statistical-review-downloads.html; last access 27 March 2015). Figure S2 shows the spatial distribution of CO_2 emissions from ODIAC re-gridded on the inversion 1-km domain over the three years (Sept. 2012-Sept. 2015). ODIAC spatial distributions were estimated at 1 × 1 km resolution (**10**). The emissions from power plants are mapped using the geolocation reported in the Carbon Monitoring and Action (CARMA) global power plant database (www.carma.org; last access 27 March 2015) and the rest of the emissions (nonpoint source emissions) are distributed using the satellite observed nightlight data. The nightlight data used in this version of ODIAC emission data were developed using a new algorithm, improving the representation of suburban areas compared to the original version (**11**). ODIAC emission data only indicate monthly emissions (based on CDIAC monthly emission data) and do not have diurnal and weekly cycles. Further details of the ODIAC are described in (**10**).

Text S5. Biogenic CO_2 fluxes: Vegetation Photosynthetic Respiration Model (VPRM-Urban). Biogenic CO_2 fluxes were estimated over Marion County, Indiana for the years 2012-2015 at hourly time step and 500 m spatial resolution using a version of the Vegetation Photosynthesis and Respiration Model (VPRM) that has been modified to represent urban ecosystems in general (**12**). VPRM is a data-driven, spatially explicit light use efficiency model that utilizes remotely sensed land surface greenness data and gridded climate data to estimate gross ecosystem carbon fluxes (gross ecosystem exchange and ecosystem respiration). The modified urban VPRM accounts for the lack of model parameters for urban ecosystems, which are typically not modeled in carbon flux products, by assuming that urban ecosystems are assemblages of impervious land cover (e.g. pavement) and the background, forested ecosystem. The model modifies the gross component carbon fluxes based on the per-pixel impervious land cover (**13**, **14**), assuming limited carbon flux through impervious surfaces (**14**). Estimated carbon fluxes from urban VPRM has been used in previous atmospheric inversion studies over Boston (**15**). Additionally, our modified urban VPRM estimates carbon fluxes for the nearby cropland, which has very different carbon exchange properties and impacts the background carbon concentration significantly. The urban VPRM incorporates the highly variable fraction of impervious surface area (ISA) from the National Land Cover Database (NLCD; **16**) in order to modulate carbon fluxes from these heterogeneous landscapes. The total CO2 fluxes over September 2012 to September 2015 are shown in Figure S3. We modeled the non-paved portions of Indianapolis as deciduous, broadleaf forest using parameters estimated from the nearby Morgan-Monroe flux tower (**17**). Our VPRM is driven by greenness data (as the Enhanced Vegetation Index) derived from the MCD43A4 MODIS product and NARR climate reanalysis (air temperature interpolated to 1-hourly time step). Emission of respired CO_2 from soil under paved surfaces is assumed to be zero, while emission of respired carbon by urban forests is reduced by the proportion ISA within a given forested pixel. Because the area around Indianapolis is predominantly cropland, which has very different carbon exchange properties than forests, we estimated sub-pixel fractions of the primary crops in the area (maize, soybeans, and pastures) based on annual, 30m data from the Cropland Data Layer (**18**) and VPRM parameters for four land cover/land use types (irrigated maize, soybeans, grasslands, and forest) (**19**), and then estimated per-pixel, hourly carbon fluxes as the weighted average of carbon fluxes for each of the four land cover/land use classes.

Text S6. The INFLUX CO_2 observation tower network. The measurement network of the INFLUX project (**20**) includes 12 sites measuring continuously CO_2 mixing ratios and 5 sites for CO mixing ratios (**21**) and shown in Fig. S4. The calibration protocol and the measurement errors have been documented previously (**22**) showing a drift of less than 0.2 ppm per year across the sites and a noise of 0.1 ppm on daily daytime averages. For the time period of this study, nine instruments were measuring CO_2 continuously and 4 measuring CO between September 2012 to July 2013. After July 2013, the full network was operational except for specific periods of time (**21**). Typical operating stations represent between 60% to 100% of the full tower network over five days. The optimization system assimilates only hourly averaged CO_2 and CO mixing ratios during daytime hours (17–22 UTC) between September 2012 and September 2015. Cavity Ring Down Spectrometer instruments (**23**) measured the atmospheric CO_2 and CO mixing ratios continuously over the period at the sampling heights varying from 40-m to 136-m above ground level. Instruments were deployed in temperature-controlled environment using existing tower infrastructures. All mixing ratio measurements have been made publicly available (**24**).

Text S7. Biogenic and sectoral contributions in atmospheric mixing ratios. Before considering the assessment of fossil fuel emissions, we present the contributions of sectoral activities and biogenic fluxes caused by the local vegetation from an atmospheric standpoint. The whole-city emissions translate into 3-ppm CO_2 enhancements (median) in winter and 1-ppm in summer, with higher observed peaks depending on wind speed and vertical mixing. These enhancements are quite small compared to day-to-day variations due to air masses crossing the continental United States carrying flux signatures from distant sources and sinks (on the order of 10-20 ppm). The fossil fuel signals further decrease in summer due to CO_2 uptake from the surrounding corn and soybean fields, grasslands and forests (Fig. S5). Hence, the critical first step for an atmospheric approach is to remove the large-scale fluctuations in CO_2 mixing ratios by measuring the background conditions. To solve that problem, three instrumented towers were deployed around Indianapolis, IN, providing background conditions for any given meteorological condition. Because background mixing ratios are inferred from rural towers upwind of the city, a local biogenic contribution is always added by the plants around each upwind site. During the growing season, the local biosphere counter-balances positive emissions signals due to carbon uptake (~3- to 4-ppm decrease) and also increases the urban enhancement in winter due to soil respiration (~0.3 ppm). Despite all these sources of uncertainties, the atmospheric model is able to simulate hourly CO_2 mixing ratios from fossil fuel and biogenic contributions within 22% of the observed enhancements averaged over 5-day periods. The use of an optimized vegetation model (**14**) and data-driven meteorological simulations (**25**) is critical to reaching such an agreement with the observations (**26**). Sectoral contributions are separated into traffic emissions (on-road and off-road) and static sources (residential, commercial, industrial, power generation, and airport), with a strong seasonality in static emissions caused by house heating and in the biogenic fluxes following the phenology of plants (Fig. S5). Fossil fuel and biospheric fluxes are spatially distinct, helping with the attribution of signals in the optimization procedure. During the growing season, the large contribution from the biosphere will inevitably limit our ability to optimize fossil fuel emissions, typically from June to August (**27**). However, the low mismatch in our simulated mixing ratios (about 20%), especially during the growing season, is promising for future deployments to detect significant discrepancies when using lower-quality biogenic or fossil fuel emission products.

Text S8. Optimization framework: Kalman Filter inversion. The inversion system used in this study is based on a Kalman Filter approach computing the exact solution of the inverse problem (analytical solution) (**5**). Compared to this study, few improvements have been implemented, all documented in other publications. The inversion solves for two sectors of emissions referred as mobile (traffic and construction engines) and static (residential, commercial, airport, energy production, and industrial) sectors, following the method described in a previous study (**28**). The optimization framework assimilates carbon monoxide (CO) mixing ratios in addition to CO_2 mixing ratios, for daytime hours (17-22 UTC). The two-specie inversion system relies on emission factors for CO and CO_2 determined from discrete flask samples collected at specific locations (**27**). Each sector of the original Hestia emission product has been assigned a CO:CO_2 ratio as described previously (**28**). Compared to previous studies (**5**), biogenic fluxes are also being optimized using the prior fluxes from VPRM. The error structures associated with each component of the state vectors (mobile, static, and biogenic) are constructed following the same methodology (**5**), using an exponentially decaying length scale (here 4km), a mask to remove correlations when sectoral emissions are equal to zero, and variances scaled relative to the prior emissions for each 1-km pixel. Power plant emissions were assigned lower uncertainties (less than 10%) as emissions from energy production is well-documented compared to other sectors (**29, 30**). Overall, the optimization system solves for 1-km resolution 5-day average daytime estimates for the three components (3x87x87=22,707 unknowns). No correlation was applied between 5-day inversion windows. An initial evaluation of the inverse emissions has been performed for October and November of 2014, comparing aircraft mass-balance estimates, the inverse solution over Indianapolis (using the exact same system described here), and a high-resolution inventory (Hestia), reconciled by removing the biogenic contribution using $^{14}CO_2$ flask measurements (**31**).

Text S9. Sensitivity experiments on power plant uncertainties. Uncertainties in prior emissions were assigned relative to the a priori emissions (100% for sectoral emissions, 30% for biogenic fluxes) and spatial structures were constructed as described in section 7 of the Supp. Info. Here, we describe the impact of assigning larger uncertainties to power plant emissions and evaluate its impact on the spatial distribution of emission adjustments. Figure S6 shows the adjustments made to sectoral prior emissions for the static (lower row) and mobile (upper row) sectors. The original configuration with low power plant uncertainties (right column) shows a distinct spatial distribution of the emission adjustments compared to high power plant uncertainties (left column). The decrease in emissions for the mobile sector in the southwestern part of the city is re-attributed to the power plant emissions when power plant emissions are highly uncertain. Similarly, the decrease in static emissions (southern and eastern part of the city) is reduced, the decrease being attributed to the power plant emissions. Overall, the power plant emissions decrease by about 35% when large uncertainties are assigned. However, uncertainties of 100% are unlikely considering the recent studies on power plant emissions compiled from two different methodologies (**29**, **30**). A comparison of the Environmental Protection Agency (EPA) estimates and the Department of Energy estimates showed a median difference of 1.2%, with a kurtosis of 24% revealing that few power plants (about 12% of the samples) exhibit differences larger than 20%. Estimates for the Harding Street power plant in Indianapolis did not reveal any large differences, which justifies the use of a low error variance in the optimization, here the median of inventory differences for US power plants.

Text S10. Dependence of optimized emissions to the granularity in prior emissions. We evaluated the sensitivity of the optimization system to granularity in the prior emissions by comparing two configurations. The first configuration is using Hestia emissions as a prior, assimilating CO_2 mixing ratios only (no CO measurements). The second configuration is identical except for the a priori emissions, here ODIAC, and the prior emission error covariance constructed according to ODIAC emissions. For this second configuration, error correlations match the coarser resolution of ODIAC, generated with the same correlation length-scale (4-km) but extending further due to the smoother spatial gradients within the urban area (diffusive nature of the nighttime satellite data). The maps of the relative adjustments for the two configurations are shown in Figure S7. When using ODIAC, an increase in prior emissions is observed, consistent with the lower whole-city emissions compared to Hestia and the original optimized emissions. Most of the urban area is increased relative to the prior except for the Harding Street power plant, slightly decreased, similar to the configuration using Hestia as a prior. This result is consistent with the prior emissions as ODIAC is using reported power plant emissions similar to Hestia. Larger correlations in the ODIAC-based prior error covariances, due to the diffuse distribution of sources, generates spurious corrections in distant urban area as seen in the northeastern corner of the optimization domain (left panel). Overall, the convergence of the two configurations shows the potential of the atmospheric optimization system (Fig. 2 in the main text) despite the lack of granularity in the prior emissions. However, no sectoral information is available (only total CO_2 emissions from ODIAC) and the spatial attribution of correction is less precise than using Hestia as a priori.

Text S11. Convergence potential estimated by perturbation experiments. We estimated the potential of convergence of the optimization system by perturbing the Hestia emissions. Based on the agreement between Hestia and the optimized emissions, the objective is to evaluate the actual constraint from the atmospheric measurements, inferring the adjustment of an incorrect prior estimate when the spatial distribution is preserved. For degraded spatial distribution, we refer to the optimization using ODIAC which amounts to adjust a 3-km resolution a priori with point sources similar to Hestia but a lower granularity for distributed sources (cf. Fig. S2 of Supp. Info.) as described in section 4 of the Supp. Info. ODIAC whole-city emissions are slightly lower than Hestia (cf. Figure 3 of the main text). The results of biased prior experiments are presented in Figure S8 with three time series showing the whole-city 5-day emissions before and after optimization (upper panel), the relative correction of the biased prior emissions in percent (middle panel), and the biogenic fluxes from Urban VPRM and after optimization (lower panel). We increased Hestia emissions by 40% corresponding to a seasonally-varying bias. The relative adjustment over 5-day periods reaches 26% (median value) with a maximum around 40% reached for about 20% of the 5-day periods. Non-convergence is not significantly correlated with meteorological variables nor data availability. We conclude here that the inversion is able to detect biases in prior emissions and reduce the systematic differences by up to 70%. A second experiment with a lower bias (+15%), discussed in the main text, shows a higher convergence similar to the original optimized emissions. During the three summer periods, the optimization shows less potential to reduce the mismatch between the prior and the original Hestia emissions due to the additional uncertainties from biogenic CO_2 fluxes in and around the city. Convergence potential is reduced by half during summers, or less than half in 2015 during which the uptake from biogenic fluxes remains smaller than 2013 and 2014. Summer of 2015 was particularly wet in Indianapolis with twice the normal amount of precipitation in June and July and very dry conditions in August and September with half the normal precipitation (compared to 1981-2010 averages, National Weather Service statistics https://www.weather.gov/ind/Precip_scorecard_IND). These unusual conditions decreased the Urban VPRM simulated uptake from the vegetation in Summer 2015 as shown in Fig. S8 (lower panel). In addition, two sector-specific experiments were conducted by introducing biases (+15%) in the Hestia prior estimates for one of the two sectors. Results are presented in Figure S9. Theoretically, and considering the agreement between the sectoral emissions in Hestia and in the optimized solution from the unbiased case, both experiments should produce unbiased optimized sectoral emissions, hence converging toward the center of the figure. Here, biases are incorrectly attributed to the complementary sector in both experiments, revealing the lack of convergence at the sectoral level despite the use of two trace gas species (CO and CO_2). Attribution of biases between the two sectors is primarily driven by uncertainties, with larger adjustments of sectoral emissions driven by larger error variances, here the mobility sector.

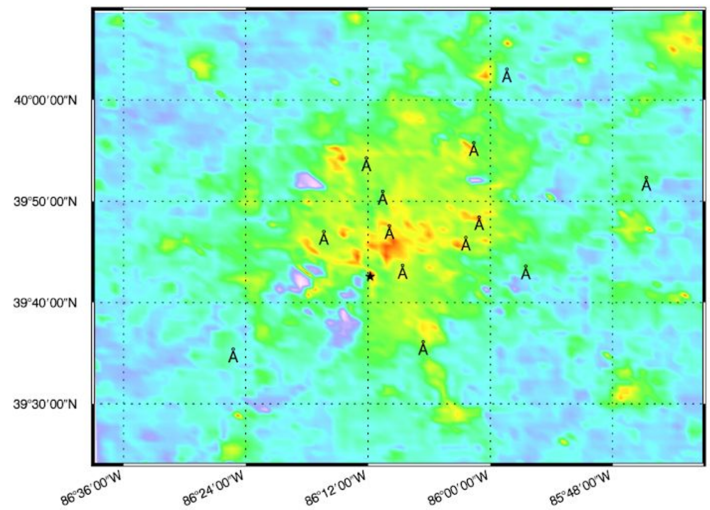

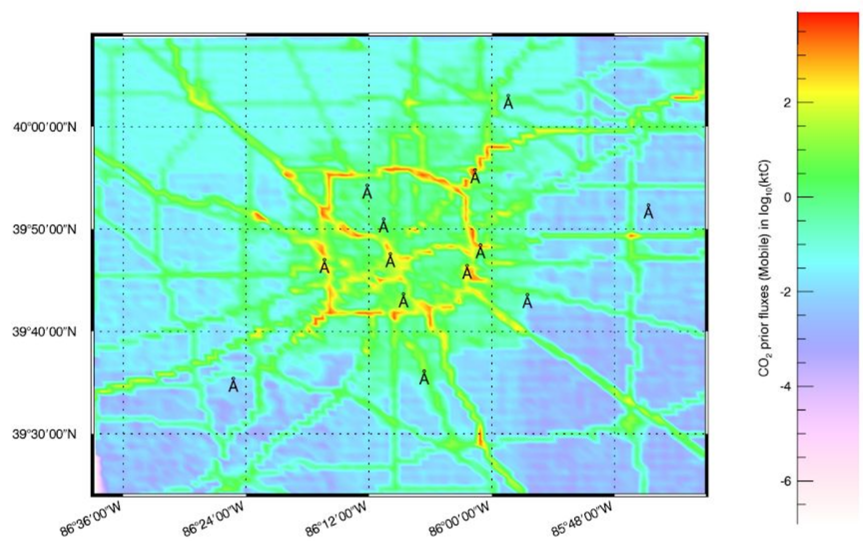

Fig. S1. Maps of the Hestia static (upper panel) and mobile (lower panel) sectoral emissions in log(ktC) over September 2012 to September 2015. The Harding Street power plant (star symbol, left panel) emissions are not correctly represented here to improve the visualization of the spatial gradients. Tower signs indicate the locations of the INFLUX tower network for CO_2 measurements.

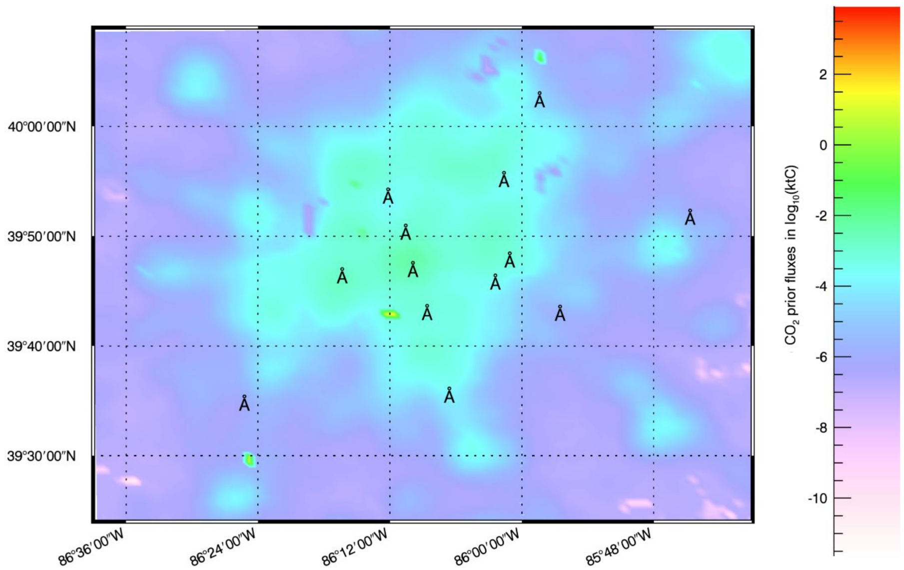

Fig. S2. Map of the ODIAC CO_2 emissions in log(ktC) over September 2012 to September 2015. The Harding Street power plant emissions are beyond the color scale to improve the visualization of the spatial gradients. Tower signs indicate the locations of the INFLUX tower network for CO_2 measurements.

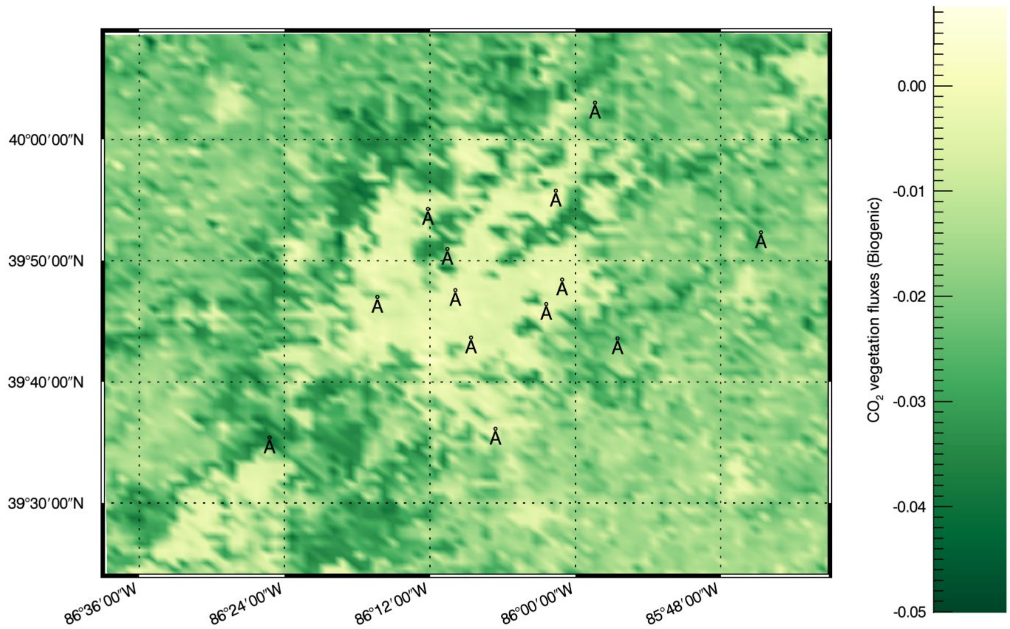

Fig. S3: Map of biogenic CO2 fluxes from Urban VPRM used in the optimization system in ktC over September 2012 to September 2015. Carbon uptake by the vegetation has been assigned a negative sign whereas release of carbon by autotrophic and heterotrophic respiration is indicated as positive. Tower signs indicate the locations of the INFLUX tower network for CO_2 measurements.

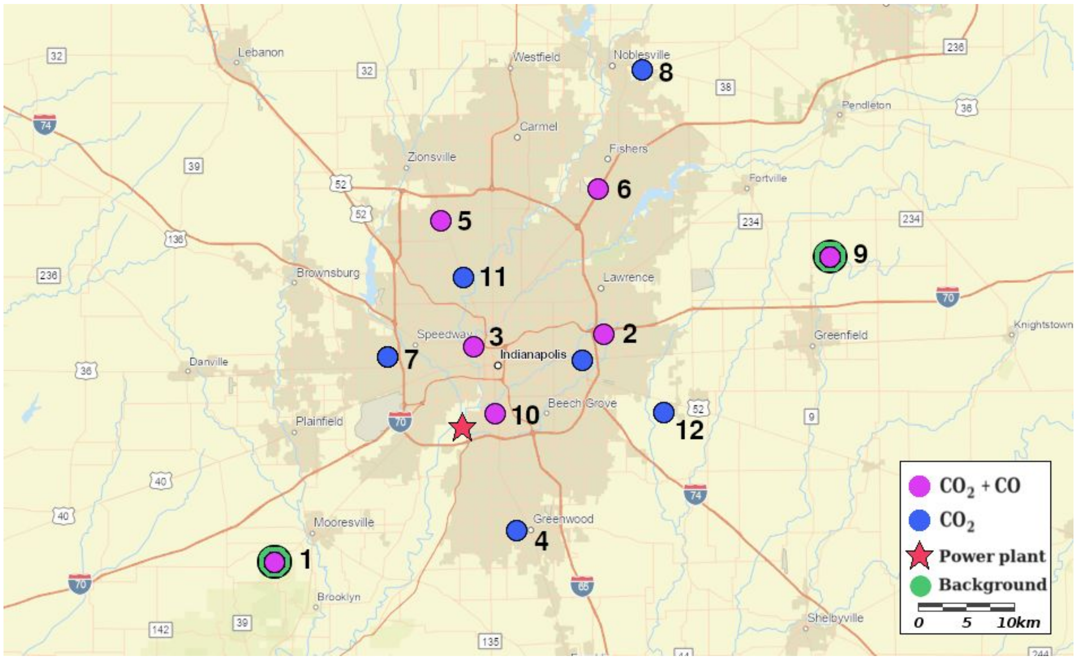

Fig. S4: Map of the instrumented tower INFLUX measurement network including sites measuring both CO_2 and CO atmospheric mixing ratios (purple circles) and sites measuring only CO atmospheric mixing ratios (blue circles). The Harding Street power plant, the largest source of CO_2 per surface area representing about 30% of the total CO_2 emissions from the domain, is indicated by a red star. Background sites are indicated by a green circle, selected for each hourly observations depending on the observed wind direction. The background of the map represents the urban area (brown), the rural area (yellow), state forest (light green), and major roads including state highways and state roads (in orange). The background was created using ArcGIS® software by Esri. ArcGIS® and ArcMap™ are the intellectual property of Esri and are used herein under license. Copyright © Esri. All rights reserved. For more information about Esri® software, please visit www.esri.com.

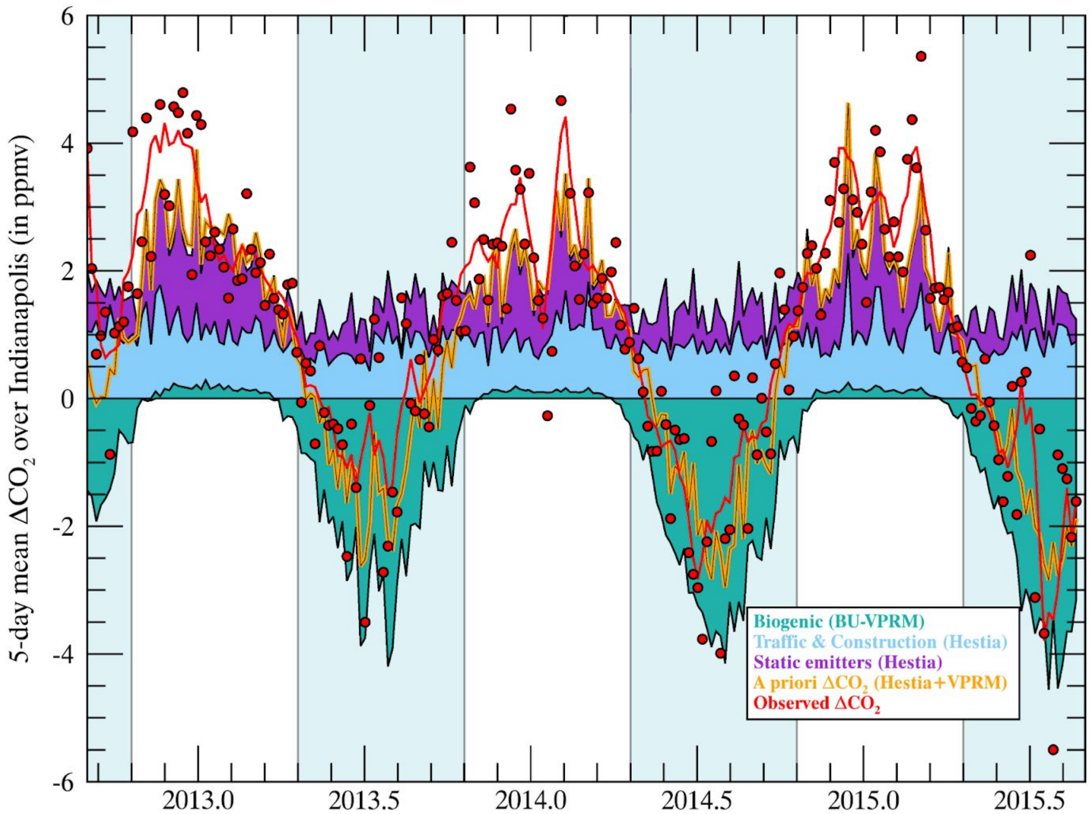

Fig. S5: Atmospheric CO_2 mixing ratio differences between upwind and downwind measurement locations (in ppm) averaged over 5-day periods for daytime only from September 2012 to September 2015. Observed atmospheric mixing ratio differences (red circles) and 2-week running averages (red line) are compared to WRF-LPDM simulations coupled to Hestia and VPRM-Urban (orange line). Simulated mixing ratio differences are shown for each individual component, i.e. mobile (in blue) and stationary (in purple) sources, and biogenic (in dark green) fluxes. Growing seasons are indicated in shaded blue areas. Negative values correspond to a net uptake of carbon between upwind and downwind sites while positive values indicate a net release of carbon into the atmosphere.

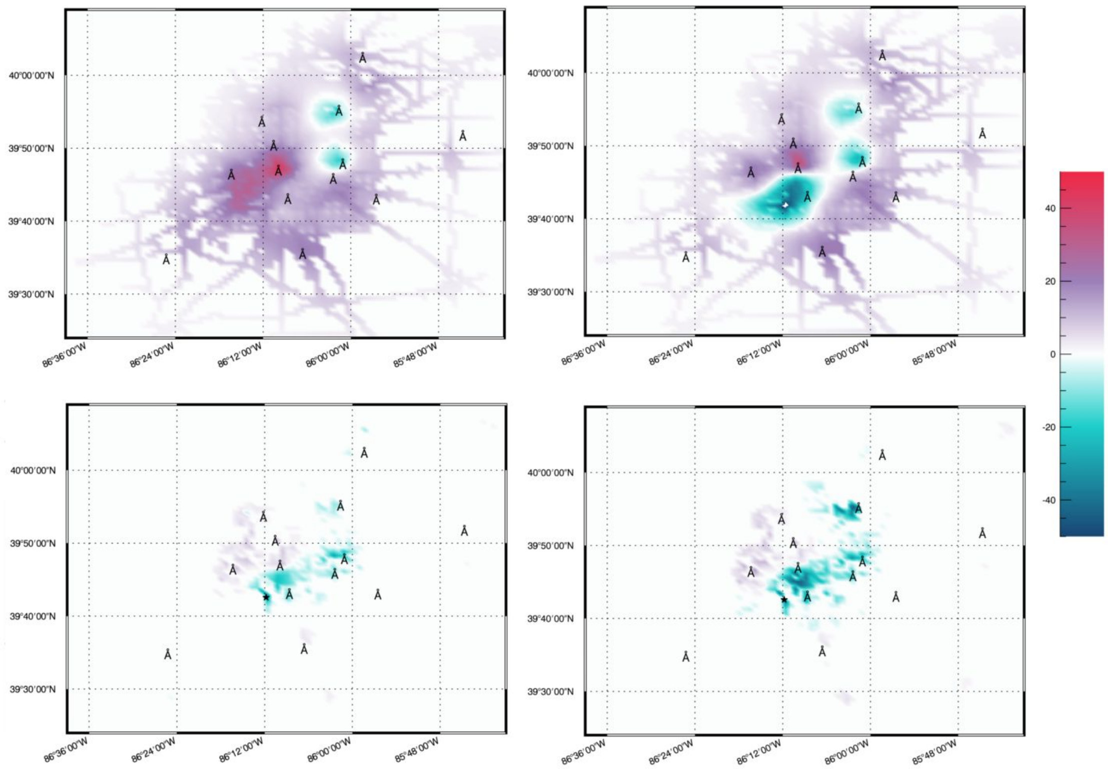

Fig. S6: Maps of the sectoral emission adjustments (in % of the prior emissions, here Hestia) for the mobile (upper row) and the stationary (lower row) sectors over 3 years (Sept. 2012 to Sept. 2015) assuming large uncertainties in power plant emissions (Harding Street power plant, star) in the error variance (left column) and low error variance in the original inversion configuration (right column). Uncertainty estimates for the Harding Street power plant correspond to median values from statistical analyses of US power plants (7). Tower signs indicate the locations of the INFLUX tower network for CO_2 measurements.

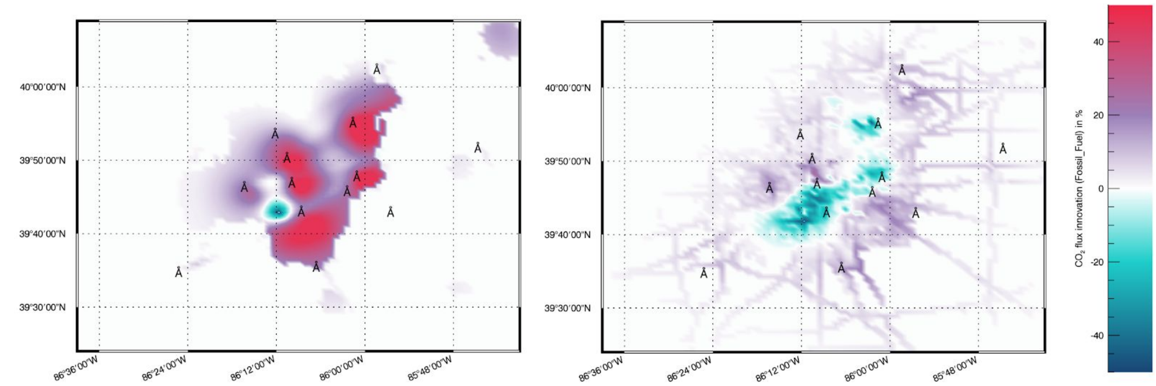

Fig. S7: Maps of the total CO_2 emission adjustments (in %) relative to prior emissions (percentage of change between prior and posterior emissions) when using Hestia emissions (right panel) and ODIAC emissions (left panel) as *a priori* in the optimization system over 3 years (Sept. 2012 to Sept. 2015). Tower signs indicate the locations of the INFLUX tower network for CO_2 measurements.

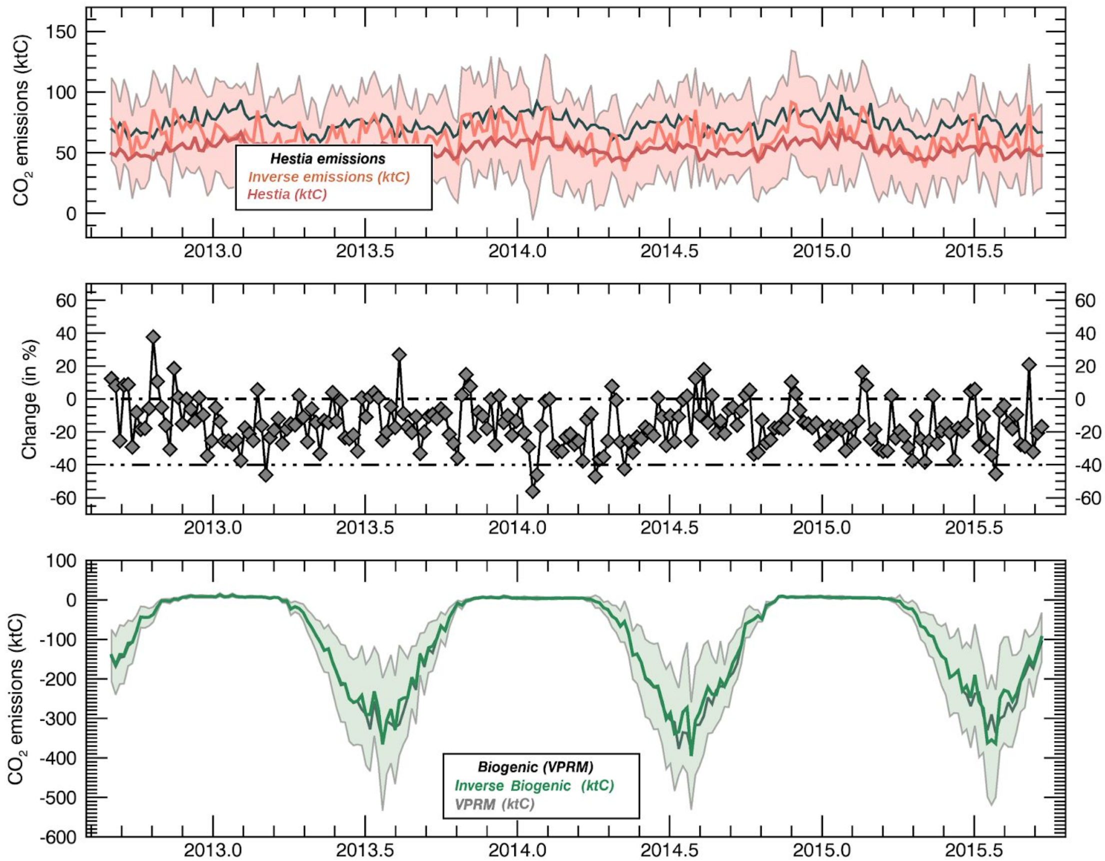

Fig. S8: Whole-city 5-day daytime (12-22 UTC) averaged CO_2 emissions from the city of Indianapolis, IN (nine counties) in ktC from September 2012 to September 2015 when using a biased prior (+40%) based on Hestia, before (black line, upper panel) and after (orange line, upper panel) optimization for the fossil fuel emissions compared to the original Hestia values (bold red line, upper panel). The adjustments after optimization (relative change in %) are shown in the middle panel with a median value of 26%. The dash-dotted line at -40% represents the relative change to match the Hestia emissions. Biogenic fluxes from Urban VPRM (in black) and after optimization (in green) are shown in the lower panel. Values correspond to the aggregated totals of 1-km resolution fluxes.

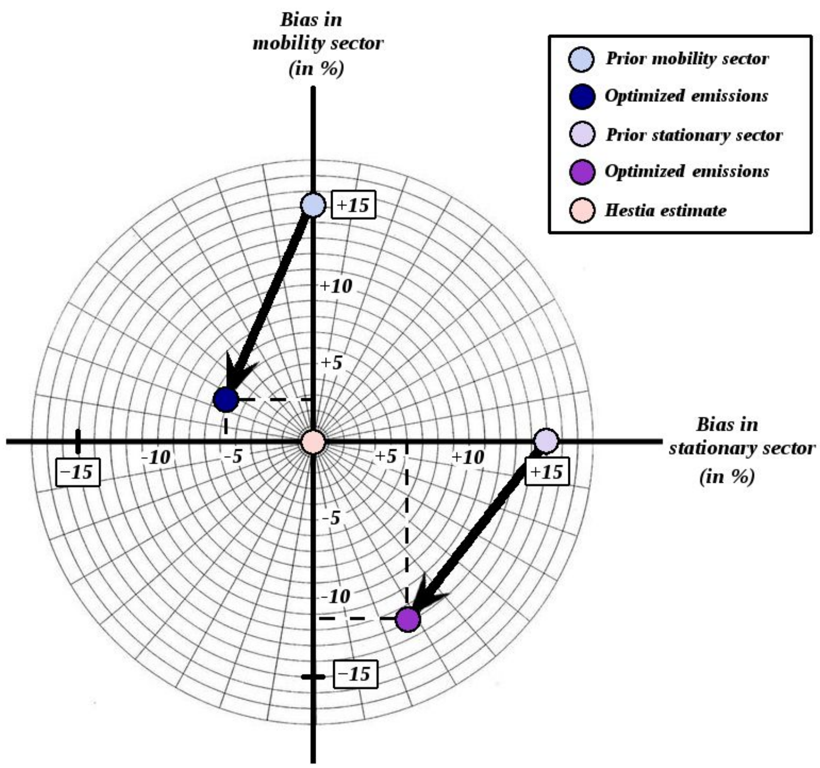

Fig. S9: Radial representation of bias removals from two sectoral bias experiments (biases are represented as fractions of the original Hestia sectoral estimates). A priori estimates were constructed by adding 15% to the Hestia sectoral estimates. The optimization procedure over the three years (September 2012 - September 2015) mis-attributes part of the original biases (only applied to the mobility or the stationary sector) to the complementary sector. The arrows represent the corrections applied to the two sectors for both experiments (mobility-only bias and stationary-only bias).

References

1. Skamarock WC, Klemp JB, Dudhia J, Gill DO, Barker DM, Duda MG, Huang X-Y, Wang W and Powers JG 2008. A description of the Advanced Research WRF Version 3. NCAR Technical Note NCAR/TN-475+STR, : 113.

2. Stauffer, D.R. and N.L. Seaman, 1994: Multiscale Four-Dimensional Data Assimilation. J. Appl. Meteor., 33, 416–434, https://doi.org/10.1175/1520-0450(1994)033<0416:MFDDA>2.0.CO;2.

3. Deng A, Stauffer DR, Gaudet BJ, Dudhia J, Hacker J, Bruyere C, Wu W, Vandenberghe F, Liu Y and Bourgeois A 2009. Update on WRF-ARW end-to-end multi-scale FDDA system. 10th Annual WRF Users' Workshop. June 23, Boulder, CO: 14.

4. Rogers, R.E., A. Deng, D.R. Stauffer, B.J. Gaudet, Y. Jia, S. Soong, and S. Tanrikulu, 2013: Application of the Weather Research and Forecasting Model for Air Quality Modeling in the San Francisco Bay Area. *J. Appl. Meteor. Climatol.,* **52**, 1953–1973, https://doi.org/10.1175/JAMC-D-12-0280.1

5. Lauvaux, T., Miles, N. L., Deng, A., Richardson, S. J., Cambaliza, M. O., Davis, K. J., Gaudet, B., Gurney, K. R., Huang, J., O'Keefe, D., Song, Y., Karion, A., Oda, T., Patarasuk, R., Razlivanov, I., Sarmiento, D., Shepson, P., Sweeney, C., Turnbull, J., Wu, K. (2016), High‐resolution atmospheric inversion of urban CO2 emissions during the dormant season of the Indianapolis Flux Experiment (INFLUX), J. Geophys. Res. Atmos., 121, 5213– 5236, doi:10.1002/2015JD024473.

6. Uliasz, M. (1994), Lagrangian particle modeling in mesoscale applications, in Environmental Modelling II, edited by P. Zanetti, pp. 71–102, Computational Mechanics Publications, Chicago, Ill.

7. Seibert, P., and A. Frank (2004), Source-receptor matrix calculation with a Lagrangian particle dispersion model in backward mode, Atmos. Chem. Phys., 4(1), 51–63, doi:10.5194/acp-4-51-2004.

8. Karion, A., Lauvaux, T., Lopez Coto, I., Sweeney, C., Mueller, K., Gourdji, S., Angevine, W., Barkley, Z., Deng, A., Andrews, A., Stein, A., and Whetstone, J.: Intercomparison of atmospheric trace gas dispersion models: Barnett Shale case study, Atmos. Chem. Phys., 19, 2561–2576, https://doi.org/10.5194/acp-19-2561-2019, 2019.

9. Gurney, K. R., I. Razlivanov, Y. Song, Y. Zhou, B. Benes, and M. Abdul‐Massih (2012), Quantification of fossil fuel CO2 emissions on the building/street scale for a large U.S. city, Environ. Sci. Technol., 46(21), 12,194–12,202, doi:10.1021/es3011282.

10. Oda, T., and S. Maksyutov (2011), A very high-resolution (1km × 1 km) global fossil fuel CO2 emission inventory derived using a point source database and satellite observations of nighttime lights, Atmos. Chem. Phys., 11(2), 543–556, doi:10.5194/acp-11-543-2011.

11. Oda, T., S. Maksyutov, and C. Elvidge (2010), Disaggregation of national fossil fuel CO2 emissions using a global power plant database and DMSP nightlight data, Proc. Asia-Pacific Adv. Network, 30, 219–228, doi:10.7125/APAN.30.24.

12. Mahadevan, P., Wofsy, S. C., Matross, D. M., Xiao, X., Dunn, A. L., Lin, J. C., ... & Gottlieb, E. W. (2008). A satellite-based biosphere parameterization for net ecosystem CO2 exchange: Vegetation Photosynthesis and Respiration Model (VPRM). Global Biogeochemical Cycles, 22(2).

13. Imhoff, M. L., Bounoua, L., Ricketts, T., Loucks, C., Harriss, R., & Lawrence, W. T. (2004). Global patterns in human consumption of net primary production. Nature, 429(6994), 870.

14. Hardiman, B. S., Wang, J. A., Hutyra, L. R., Gately, C. K., Getson, J. M., & Friedl, M. A. (2017). Accounting for urban biogenic fluxes in regional carbon budgets. Science of The Total Environment, 592, 366-372.

15. Sargent, M., Barrera, Y., Nehrkorn, T., Hutyra, L. R., Gately, C. K., Jones, T., McKain, K., Sweeney, C., Hegarty, J., Hardiman, B., Wang, J. A., and Wofsy, S. C. (2018). Anthropogenic and biogenic CO2 fluxes in the Boston urban region. Proceedings of the National Academy of Sciences, 115(29), 7491-7496.

16. Homer, C., Dewitz, J., Yang, L., Jin, S., Danielson, P., Xian, G., Coulston, J., Herold, N., Wickham, J., and K. Megown (2015). Completion of the 2011 National Land Cover Database for the conterminous United States–representing a decade of land cover change information. Photogrammetric Engineering & Remote Sensing, 81(5), 345-354.

17. Hilton, T. W., Davis, K. J., Keller, K., and Urban, N. M.: Improving North American terrestrial CO2 flux diagnosis using spatial structure in land surface model residuals, Biogeosciences, 10, 4607–4625, https://doi.org/10.5194/bg-10-4607-2013, 2013.

18. Boryan, C., Yang, Z., Mueller, R., & Craig, M. (2011). Monitoring US agriculture: the US department of agriculture, national agricultural statistics service, cropland data layer program. Geocarto International, 26(5), 341-358.

19. Hilton, T. W., Davis, K. J., & Keller, K. (2014). Evaluating terrestrial CO2 flux diagnoses and uncertainties from a simple land surface model and its residuals. Biogeosciences, 11(2), 217.

20. Davis, K.J., Deng, A., Lauvaux, T., Miles, N.L., Richardson, S.J., Sarmiento, D.P., Gurney, K.R., Hardesty, R.M., Bonin, T.A., Brewer, W.A., Lamb, B.K., Shepson, P.B., Harvey, R.M., Cambaliza, M.O., Sweeney, C., Turnbull, J.C., Whetstone, J. and Karion, A., 2017. The Indianapolis Flux Experiment (INFLUX): A test-bed for developing urban greenhouse gas emission measurements. *Elem Sci Anth*, 5, p.21. DOI: http://doi.org/10.1525/elementa.188

21. Miles, N.L., S.J. Richardson, K.J. Davis, T. Lauvaux, A. Deng, J. Turnbull, A. Karion, C. Sweeney, K.R. Gurney, R. Patarasuk, I. Razlivanov, M.O. Cambaliza, P. Shepson: Quantification of urban atmospheric boundary layer greenhouse gas dry mole fraction enhancements: Results from the Indianapolis Flux Experiment (INFLUX). Elem Sci Anth., 5:27, doi: 10.1525/elementa.127, 2017.

22. Richardson SJ, Miles NL, Davis KJ, Lauvaux T, Martins DK, Turnbull JC, K McKain, C Sweeney, M O L. Cambaliza: Tower measurement network of in-situ CO2, CH4, and CO in support of the Indianapolis FLUX (INFLUX) Experiment. Elem Sci Anth. 2017;5:59. DOI: http://doi.org/10.1525/elementa.140

23. Crosson, E. R. (2008), A cavity ring-down analyzer for measuring atmospheric levels of methane, carbon dioxide, and water vapor, Appl. Phys. B, 92(3), 403–408.

24. Miles, N.L.,S.J. Richardson, K.J. Davis, and B.J. Haupt, 2017. In-situ tower atmospheric measurements of carbon dioxide, methane and carbon monoxide mole fraction for the Indianapolis Flux (INFLUX) project, Indianapolis, IN, USA. Data set. Available on-line [http://datacommons.psu.edu] from The Pennsylvania State University Data Commons, University Park, Pennsylvania, USA. http://dx.doi.org/10.18113/D37G6P.

25. Deng, A., Lauvaux, T., Davis, K.J., Gaudet, B.J., Miles, N., Richardson, S.J., Wu, K., Sarmiento, D.P., Hardesty, R.M., Bonin, T.A., Brewer, W.A. and Gurney, K.R., 2017. Toward reduced transport errors in a high resolution urban CO2 inversion system. *Elem Sci Anth*, 5, p.20. DOI: http://doi.org/10.1525/elementa.133

26. Lian, J., Wu, L., Bréon, F.-M., Broquet, G., Vautard, R., Zaccheo, T.S., Dobler, J. and Ciais, P., 2018. Evaluation of the WRF-UCM mesoscale model and ECMWF global operational forecasts over the Paris region in the prospect of tracer atmospheric transport modeling. *Elem Sci Anth*, 6(1), p.64. DOI: http://doi.org/10.1525/elementa.319

27. Turnbull, J. C., C Sweeney, A. Karion, T. Newberger, S. J. Lehman, P. P. Tans, K. J. Davis, T. Lauvaux, N. L. Miles, S. J. Richardson, M. O. Cambaliza, P. B. Shepson, K. R. Gurney, R. Patarasuk, and I. Razlivanov (2015), Toward quantification and source sector identification of

fossil fuel CO2 emissions from an urban area: Results from the INFLUX experiment, *J. Geophys. Res. Atmos.*, 120, 292– 312, doi:10.1002/2014JD022555.

28. Nathan, B. J., Lauvaux, T., Turnbull, J. C., Richardson, S. J., Miles, N. L., & Gurney, K. R. (2018). Source sector attribution of CO2 emissions using an urban CO/CO2 Bayesian inversion system. *Journal of Geophysical Research: Atmospheres*, 123, 13,611– 13,621. https://doi.org/10.1029/2018JD029231

29. Gurney, K. R., Huang, J. and K Coltin (2016). Bias present in US federal agency power plant CO2 emissions data and implications for the US clean power plan, Environ. Res. Lett., 11, 064005, https://doi.org/10.1088/1748-9326/11/6/064005

30. Quick, J.C., and E. Marland (2019) Systematic error and uncertain carbon dioxide emissions from U.S. power plants, Journal of the Air & Waste Management Association, 69:5, 646-658, DOI: 10.1080/10962247.2019.1578702

31. Turnbull, J., Karion, A., Davis, K. J., Lauvaux, T., Miles, N.L., Richardson, S. R., Sweeney, C., McKain, K., Lehman, S., Gurney, K.R., Patarasuk, R., Liang, J., Shepson, P., Heimburger, A., Harvey, R., and Whetstone, J. (2018): Synthesis of urban CO2 emission estimates from multiple methods from the Indianapolis Flux Project (INFLUX), Environmental Science & Technology **2019** *53* (1), 287-295, DOI: 10.1021/acs.est.8b05552.